

# Measurement report: Vehicle-based Multi-lidar Observational Study of the Effect of Meteorological Elements on the Three-dimensional Distribution of Particles in the Western Guangdong–Hong Kong–Macao Greater Bay Area

Xinqi Xu<sup>1,2</sup>, Jielan Xie<sup>1,2</sup>, Yuman Li<sup>1,2</sup>, Shengjie Miao<sup>1,2</sup>, and Shaojia Fan<sup>1,2</sup>

<sup>1</sup>School of Atmospheric Sciences, Sun Yat-sen University, Zhuhai, 519082, China

<sup>2</sup>Guangdong Provincial Observation and Research Station for Climate Environment and Air Quality Change in the Pearl River Estuary, Key Laboratory of Tropical Atmosphere-Ocean System, Ministry of Education, Southern Marine Science and Engineering Guangdong Laboratory (Zhuhai), Zhuhai, 519082, China

*Correspondence to:* Shaojia Fan (eesfsj@mail.sysu.edu.cn)

**Abstract:** The distribution of meteorological elements has always been an important factor in determining the horizontal and vertical distribution of particles in the atmosphere. To study the effect of meteorological elements on the three-dimensional distribution structure of particles, mobile vehicle lidar, and fixed-location observations were collected in the western Guangdong–Hong Kong–Macao Greater Bay Area of China during September and October in 2019 and 2020. Vertical aerosol extinction coefficient, depolarization ratio, and wind and temperature profiles were measured using a micro pulse lidar, a Raman scattering lidar, and a Doppler wind profile lidar installed on a mobile monitoring vehicle. The mechanism of how wind and temperature in the boundary layer affects the horizontal and vertical distribution of particles was analysed. The results shows that particles were mostly distributed in downstream areas on days with moderate wind speed in the boundary layer, whereas they were distributed homogeneously on days with weaker wind. There are three typical types of vertical distribution of particles in the western Guangdong–Hong Kong–Macao Greater Bay Area (GBA): surface single layer, elevated single layer, and double layer. Analysis of wind profiles and Hybrid Single-Particle Lagrangian Integrated Trajectory Model (HYSPLIT) backward trajectory reveals different sources of particles for the three types. Particles concentrating near the temperature inversion and multiple inversions could cause more than one peak in the extinction coefficient profile. There were two mechanisms affecting the distribution of particulate matter in the upper and lower boundary layers. Based on this observational study, a general model of meteorological elements affecting the vertical distribution of urban particulate matter is proposed.

## 1. Introduction

The Guangdong–Hong Kong–Macao Greater Bay Area (GBA) is one of China’s national key economic development regions. It consists of Guangzhou (GZ), Shenzhen (SZ), Zhuhai (ZH), Foshan (FS), Huizhou (HZ), Dongguan (DG), Zhongshan (ZS), Jiangmen (JM), and Zhaoqing (ZQ) in Guangdong province, as well as Hong Kong and Macao, the two Special Administrative Regions.

37 Covering 56,000 square kilometres, the GBA had a vast population of over 70 million at the end of  
38 2018. The GBA plays a significant role in boosting global trade along the land-based Silk Road  
39 Economic Belt and the 21st Century Maritime Silk Road. With the rapid development of the regional  
40 economy, increasingly more studies on air quality and climate effect in the GBA have also been  
41 conducted (Fang et al., 2018; Shao et al., 2020; Zhou et al., 2018).

42  
43 Anthropogenic particles in the air play an important role in the environment of human living. They not  
44 only act as air pollutants posing harmful effects to human health (Liao et al., 2017; Leikauf et al., 2020;  
45 Yao et al., 2020; Orru et al., 2017) but also alter the temperature near the ground owing to their ability  
46 to absorb and scatter solar radiation (IPCC, 2014; Strawa et al., 2010). As a result of industrialisation  
47 and urbanisation, megacity clusters in China such as the Beijing–Tianjin–Hebei [also called Jing-Jin-Ji  
48 (JJJ) in Chinese] area, Yangtze River Delta (YRD), and Guangdong–Hong Kong–Macao GBA, have  
49 been seriously affected by particulate matter in recent years. Numerous studies on the particulate matter  
50 have been conducted in these areas (Xu et al., 2018; Liu et al., 2017; Du et al., 2017). Particles in the  
51 boundary layer can, directly and indirectly, affect human lives and activities. Therefore, it is essential  
52 to study their distribution characteristics.

53  
54 The distribution of particles is influenced not only by changes in source emissions but also by changes  
55 in meteorological factors such as temperature and wind. It has previously been observed that a low  
56 boundary layer height and complex vertical distributions of aerosols, temperature, and relative  
57 humidity are the main structural characteristics of haze days (Huige et al., 2021). Previous studies have  
58 confirmed that different types of temperature inversions have different impacts on particles in the  
59 boundary layer (Wallace et al., 2009; Wang et al., 2018). The depth and temperature difference of the  
60 inversion region is a key factor for predictions of surface PM<sub>2.5</sub> concentrations (Zang et al., 2017). It  
61 has been previously observed that wind fields play an important role in transboundary-local aerosol  
62 interactions (Huang et al., 2021a; Huang et al., 2021b). Recent evidence suggests that wind shear is an  
63 important factor in terms of PM<sub>10</sub> vertical profile modification (Sekula et al., 2021). The concentration  
64 of particulate matter also shows characteristics of wind-dependent spatial distributions in which  
65 pollutant transport within the GBA city cluster is significant (Xie et al., 2019). Hence, the issue of how  
66 meteorological factors affect the distribution of particles has received considerable critical attention.

67  
68 Lidar is an active remote sensing device. It emits a laser light beam and receives a backscatter signal,  
69 which can be further used to retrieve the vertical distribution of particle optical properties, wind, and  
70 temperature. It has been widely applied in the fields of meteorology and environmental science. In  
71 most studies, it is used as a ground-based or satellite-based instrument (Tian et al., 2016; Liu et al.,  
72 2017; Heese et al., 2017).

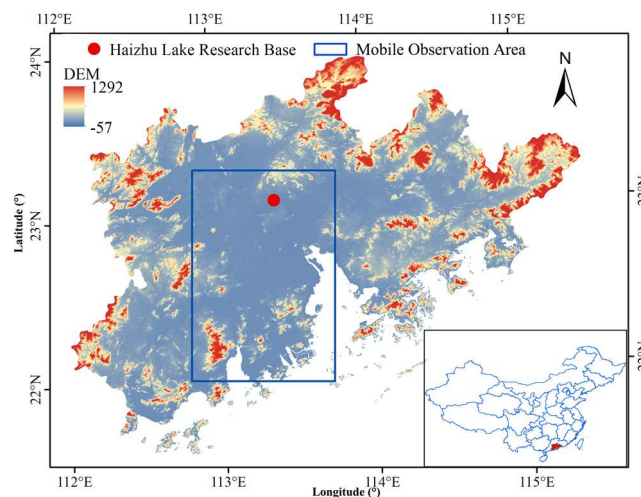
73  
74 In recent years, vehicle-based lidar observation has been gradually developed and become a powerful  
75 tool to detect the physical and chemical properties of the boundary layer. Compared with traditional  
76 observations, it can carry out continuous mobile observations and obtain the change of vertical profiles  
77 of certain factors in its path. Additionally, a mobile lidar system can be used to conduct supplementary  
78 observations in areas with no lidar present. In the past few years, several vehicle-based observational  
79 experiments have been carried out (Lv et al., 2017; Lyu et al., 2018; Lv et al., 2020; Zhao et al., 2021;  
80 Fan et al., 2018), but research aimed at multi-lidar observations and the effect of the vertical structure

81 of meteorological factors on the distribution of particles has largely been an underexplored domain,  
82 especially in the GBA. Former research revealed that pollution of particulate matter frequently occurs  
83 in the western part of inland regions of GBA (Fang et al., 2019), affecting downstream cities under the  
84 northerly wind field. Hence, the authors were motivated to perform observations in the western GBA  
85 with a multi-lidar system installed on a vehicle to study the influence of the three-dimensional structure  
86 of meteorological elements on the distribution of particles.

## 87 2. Data and Method

### 88 2.1 Description of Observations

89 The horizontal distribution of the particles was studied by making mobile vehicle lidar observations  
90 over the west bank of the Pearl River Estuary. During the mobile vehicle lidar observations experiment,  
91 the vehicle was driven clockwise along the west bank of the Pearl River Estuary, passing through main  
92 cities of the GBA in the route, from as far north as Guangzhou to as far south as Zhuhai. The total  
93 length of the route was approximately 320 km, and the experiment was conducted during the daytime.  
94 The vehicle-based observation lasted for seven continuous days, which started on August 29th and  
95 ended on September 4th, 2020. During most of the mobile observations, the relative humidity of  
96 Zhuhai, the closest city to the sea, was below 60 %. Therefore, the influence of hygroscopic growth on  
97 the extinction coefficient was negligible. To study the vertical distribution of the particles, we  
98 conducted fixed-location lidar observation experiments using the same lidar system from September  
99 10th to October 8th, 2019, and from August 29th to October 27th, 2020, totalling 89 days. The reason  
100 for choosing these periods is that they include the wet season change to the dry season in the GBA area.  
101 Therefore, changes in meteorological elements have a significant impact on the three-dimensional  
102 distribution of particles. The location of the Haizhu Lake Research Base and the area of the measuring  
103 path are shown in Fig. 1. The research area is on the Pearl River Delta Plain. This area is bordered by  
104 the Nanling Mountains in the north. Mountain obstruction makes the GBA area less susceptible to  
105 long-distance transport of pollutants from other areas, and the transport of pollutants mainly occurs  
106 between cities in the research area. Observations with the vehicle-based multi-lidar system are listed in  
107 Table 1.  
108



109

110 **Figure 1. Location of the Haizhu Lake Research Base and the mobile observation area.**

111

112 **Table 1. Observations with the vehicle-based multi-lidar system**

Time	Observation
Sept. 10th – Oct. 8th, 2019	Fixed-location observation
Aug. 29th – Sept. 4th, 2020, in the daytime	Mobile observation
Aug. 29th – Sept. 4th, 2020, at night	Fixed-location observation
Sept. 5th – Oct. 27th, 2020	Fixed-location observation

113

## 114 2.2 Multi-lidar System

115 A multi-lidar system was installed on a vehicle in this experiment. The car used was a modified 7-  
116 seater Mercedes-Benz sport utility vehicle. Three lidars were fixed to the rear of the car by steel bars to  
117 ensure their stability. To avoid the impact of frequent changes in speed and vehicle bumps during the  
118 observation, the routes of mobile observations were basically flat highways, and the driving speed was  
119 controlled within 80 km/h. During fixed-location observations, the car was parked in the observation  
120 field and connected to a stable power source. The lidar system included a 3D visual scanning micro  
121 pulse lidar (EV-Lidar-CAM, EVERISE Company, Beijing,  
122 <http://www.everisotech.com.cn/products/ygtc/evlidarportable.html>), a twirling Raman temperature  
123 profile lidar (TRL20, EVERISE Company, Beijing,  
124 <http://www.everisotech.com.cn/products/ygtc/templidar.html>), a Doppler wind profile lidar  
125 (Windview10, EVERISE Company, Beijing,  
126 <http://www.everisotech.com.cn/products/ygtc/windview10.html>), a global positioning system (GPS),  
127 and a signal acquisition unit. The three lidars are characterised by high temporal and spatial resolution  
128 and can effectively determine the evolution of the vertical distribution of particles, as well as  
129 temperature, wind speed, and wind direction over time. The quality of data from the lidar system was  
130 checked before using in our study. Results show that the percentage difference between data provided  
131 by the lidar system and data from the Shenzhen meteorological tower was less than 15%, which  
132 indicates a sufficient accuracy of the lidar instrument. We have used this lidar system in our previous  
133 research and showed it to be reliable (He et al., 2021a; He et al., 2021b). The vehicle setup is shown in  
134 Figure 2. Details of the three lidars are shown in Table 2.

135



136

137 **Figure 2. Setup of the multi-lidar system on the vehicle.**

138

139 **Table 2. Detailed parameters for the three lidars.**

Lidar	Variable	Laser source	Wave length	Laser frequency	Spatial resolution	Time resolution
Micro pulse lidar	Original signal, Extinction coefficient profiles, Depolarization ratio profiles, Aerosol optical depth	Nd:YAG laser	532 nm	2500 Hz	15 m	1 min
Raman temperature profile lidar	Temperature profiles	Nd:YAG laser	532 nm	20 Hz	60 m	5 min
Doppler wind profile lidar	Wind speed profiles, Wind direction profiles	Fibre pulse laser	1545 nm	10 kHz	50 m	1 min

140

141 **2.3 Calculation of Extinction Coefficient and Depolarization Ratio**

142 The aerosol extinction coefficient represents the reduction of radiation in a band owing to scattering  
 143 and absorption by aerosols (Li et al., 2020). The formula for the extinction coefficient calculation  
 144 (Fernald, 1984) is as follows:

145

$$146 \quad \alpha_a(z) = -\frac{S_a}{S_m} \alpha_m(z) + \frac{P(z)z^2 \cdot \exp\left[2\left(\frac{S_a}{S_m}-1\right) \int_z^{z_c} \alpha_m(z) dz\right]}{\frac{P(z_c)z_c^2}{\alpha_a(z_c) + \frac{S_a}{S_m} \alpha_m(z_c)} + 2 \int_z^{z_c} P(z)z^2 \exp\left[2\left(\frac{S_a}{S_m}-1\right) \int_z^{z_c} \alpha_m(z) dz\right] dz} \quad (1)$$

147

148 where  $P(z)$  is the power received at altitude  $z$ ,  $\alpha_a$  and  $\alpha_m$  the particle extinction and molecular  
 149 extinction, respectively and  $S_a = 50$  Sr the particle extinction-to-backscatter ratio, which is the  
 150 default value given by the manufacturer. This value is consistent with prior work in the GBA area (Li et  
 151 al., 2020).  $S_m = 8\pi/3$  is the molecular extinction-to-backscatter ratio, and  $z_c$  the calibration height  
 152 of the micro pulse lidar, which is variable, ranging from 10-15 km, and depending on the signal  
 153 intensity.

154

155 The micro pulse lidar (MPL) system uses the scattering of polarized light to distinguish between  
 156 spherical and non-spherical particles to ascertain the particle species (Li et al., 2020). The  
 157 depolarization ratio is calculated with the following formula:

158

$$159 \quad \delta = k \frac{P_{\perp}}{P_{\parallel}} \quad (2)$$

160

161 where  $P_{\perp}$  and  $P_{\parallel}$  represent the cross-polarized and co-polarized signal, respectively.  $k$  the  
 162 depolarization calibration constant, which is the ratio of the gains of the parallel and perpendicular  
 163 channels (Dai et al., 2018).

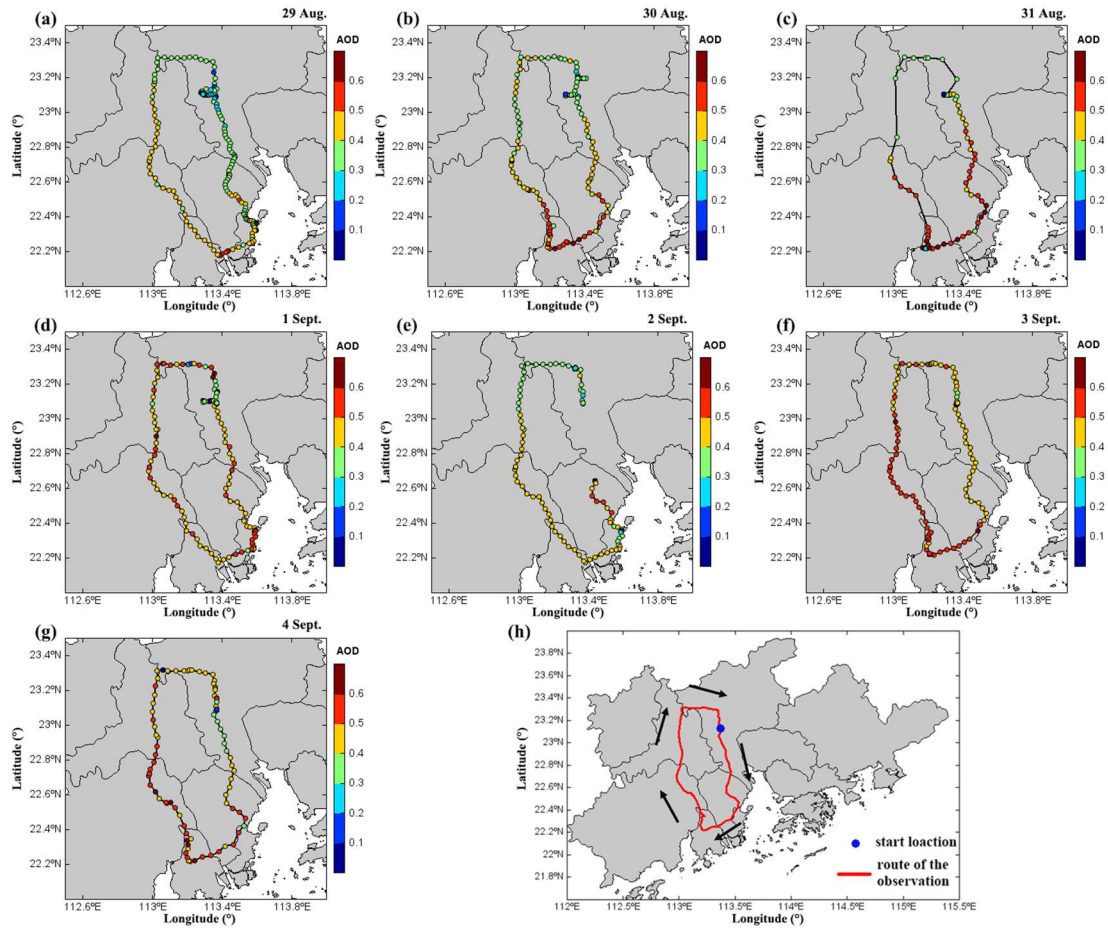
## 164 2.4 HYSPLIT Backward Trajectory Model

165 The regional transport of particulate matter was studied using the National Oceanic and Atmospheric  
166 Administration Hybrid Single-Particle Lagrangian Integrated Trajectory Model (HYSPLIT) so as to  
167 determine the trajectory of air masses. It has been widely used in the field of air masses and pollutant  
168 source analysis (Deng et al., 2016; Lu et al., 2018; Kim et al., 2020). In this study, meteorological data  
169 of the Global Data Assimilation System (GDAS) at the spatial resolution of  $0.25^\circ$  was used. To obtain  
170 the sources of particulate matter at different heights, altitudes of 100 m, 500 m, and 1000 m were set as  
171 the ending points of the trajectories.

## 172 3. Results and Discussion

### 173 3.1 Mobile Vehicle Lidar Observations

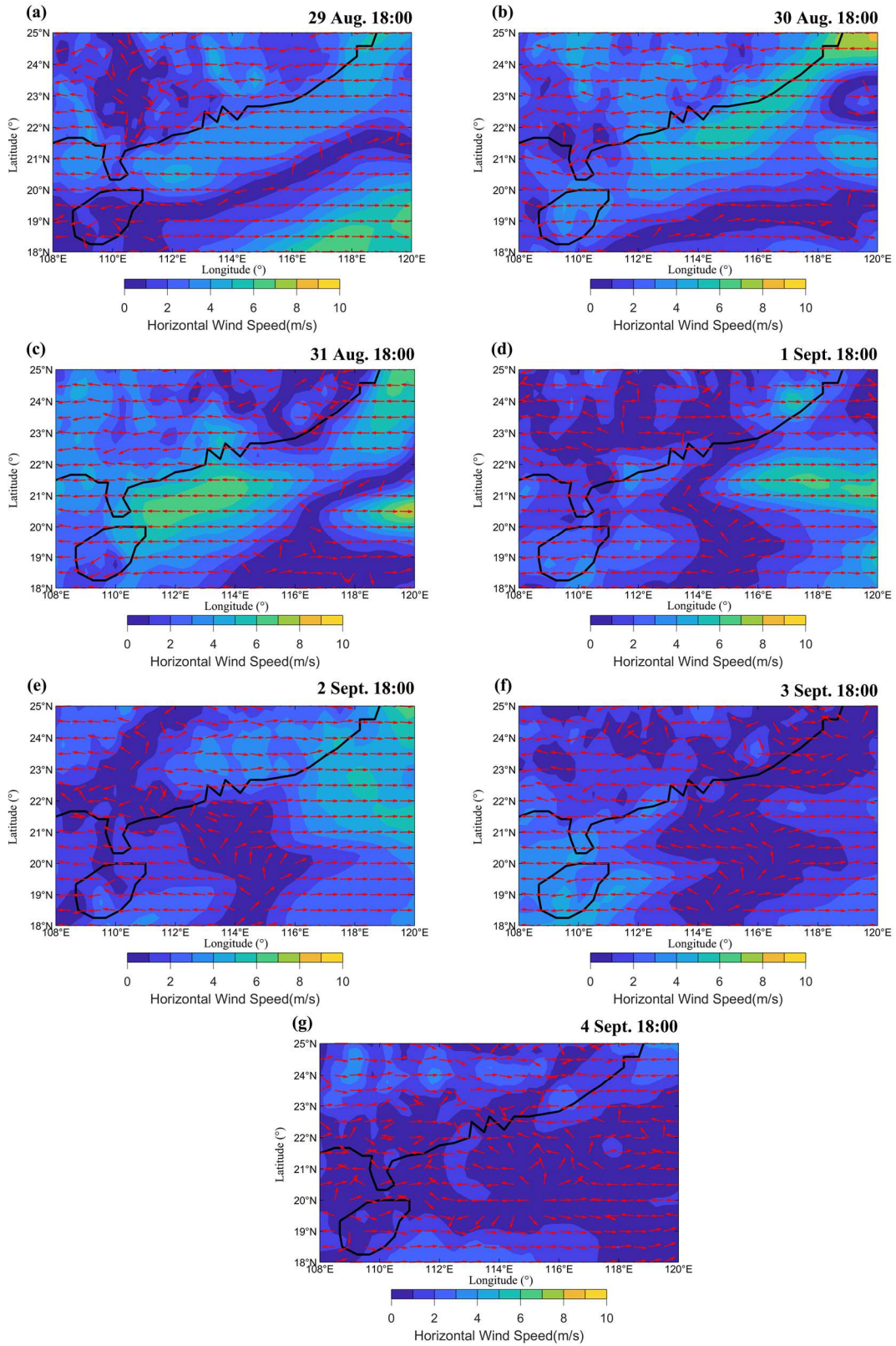
174 The horizontal distribution of particles was obtained by conducting mobile vehicle lidar observations in  
175 the GBA. The reason for choosing this route is that it covers the major urban agglomerations in the  
176 western part of the Guangdong–Hong Kong–Macao Greater Bay Area, which contains a large number  
177 of anthropogenic aerosol emission sources. It is representative of the regional distribution of particles  
178 in this area. We conducted mobile observations once a day, from August 29th to September 4th, 2020.  
179 The set off time was at 10:00 and a single measurement circle was completed at around 16:00. Owing  
180 to surface heating, convection in the boundary layer develops vigorously during daytime, which allows  
181 aerosols to mix well and form a more homogeneous vertical distribution. Therefore, mobile  
182 observations during the daytime are more appropriate to study the horizontal distribution of particles in  
183 the GBA area. Figure 3 shows the aerosol optical depth (AOD) measured with the MPL in the route.  
184 Because of GPS signal interference, some GPS data on August 31st and September 2nd were missing.  
185 On most days, sections with high AOD values fell geographically into the south and west sides of the  
186 observation region. Figure 4 shows low-level horizontal wind fields on 925 hPa over the region based  
187 on ERA5 reanalysis data. In the first three days, the wind speed over the GBA was generally higher,  
188 with an easterly and north easterly direction. Polluted aerosols were transported along with the wind to  
189 the west and south of the study area. They accumulated in the downstream area, resulting in a high  
190 value of AOD. On September 1st, 3rd, and 4th, the GBA was in an area of low wind speed, which was  
191 not conducive to the regional transport of particulate matter. As a result, the AOD value of the whole  
192 GBA reached a higher level, of which the increase in AOD in the northern region was more obvious.  
193 AOD values on these days distributed more homogeneously than days with higher wind speed. On  
194 September 2nd, the lower winds of the GBA turned westerly when the observation area in the east was  
195 downstream, and the highest points of the AOD value also appeared on the eastern route. Such results  
196 show that the horizontal distribution of particles in the GBA was closely related to wind speed and  
197 wind direction.



198  
 199  
 200  
 201  
 202

Figure 3. (a)-(g) Aerosol optical depth (AOD) measured with the MPL in the route from August 29th to September 4th, 2020, and (h) Guangdong–Hong Kong–Macao Greater Bay Area and route details.





203

204

205 **Figure 4. (a)-(g) Wind field of 925 hPa from August 29th to September 4th, 2020. The colour map represents**

206 **horizontal wind speed (m/s). Red arrows represent the wind direction.**

207

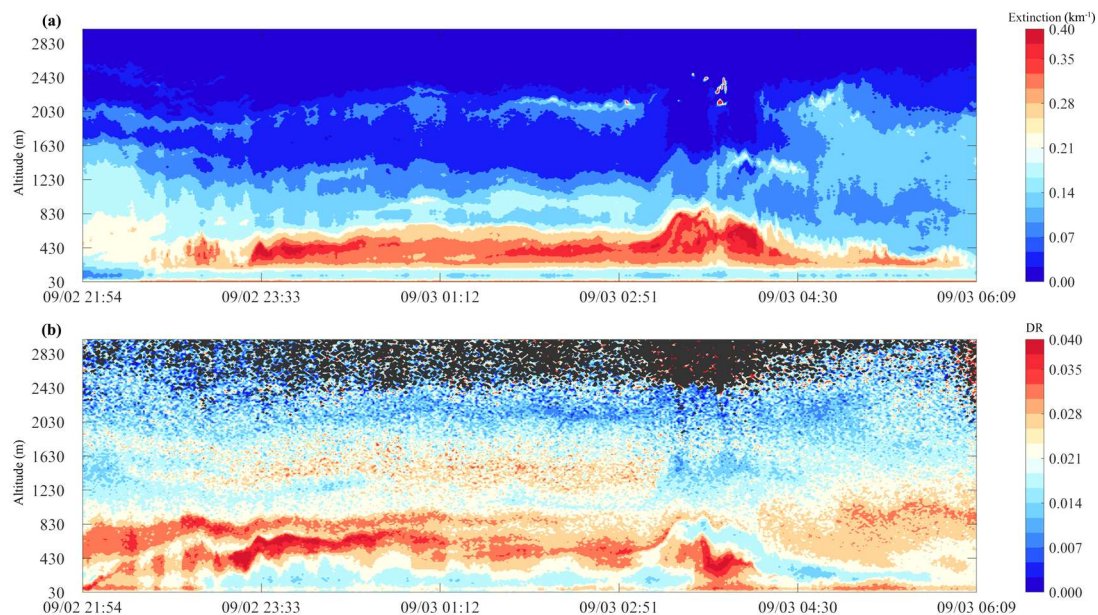


## 208 3.2 Fixed-location Lidar Observations

209 To obtain the vertical distribution of particles, fixed-location lidar observations were conducted at the  
210 Haizhu Lake Research Base, which is located in the centre of the metropolis Guangzhou. The research  
211 base is representative of the distribution of urban aerosols. Unfortunately, there is no remote sensing  
212 device in the base. This motivated us to park the car in the base and conduct a total of 89 days of fixed-  
213 location observation. During this period, we found that the hierarchical structure of aerosols occurred  
214 more frequently at night, and most of the vertical aerosol distributions are consistent with three  
215 distribution types. Therefore, we selected the three most representative processes for analysing the  
216 three distribution types. Three different vertical distribution types of particles are given below, as well  
217 as the corresponding vertical observation results of temperature and wind in the same period. Altitude  
218 values in the following figures refer to the altitude above instrument.

### 219 3.2.1 Type I: Surface Single Layer

220 On September 3rd, 2020, a clear night in autumn, the lidar system operated from 2154 to 0609 local  
221 time (LT) the next day. Figure 5(a) shows the time series of the extinction coefficient of a single aerosol  
222 layer on the surface, which was observed with the MPL. Before 0300 LT, particles accumulated below  
223 800 m. The maximum value of the extinction coefficient near the ground was between 0.3–0.5. During  
224 0300 LT and 0400 LT, there is a significant increase in the maximum height of the particle layer. After  
225 0430 LT, the maximum height of the particle layer dropped, and the near-ground extinction coefficient  
226 fell below 0.3. Figure 5(b) shows the time series of corresponding depolarization ratio profiles. Most of  
227 the depolarization ratios were below 0.1, consistent with previous research on the GBA (Tian et al.,  
228 2017). A layer of elevated depolarization ratio was visible near the boundary of the surface single layer  
229 in Figure 5(b). It can be seen that during 0300 LT and 0400 LT, there was a significant hierarchical  
230 structure with a high depolarization ratio layer near the ground and another layer of high value above.  
231 A layer with a lower value of depolarization ratio existed between the two layers with a higher value.  
232 This result indicated that there might be local anthropogenic emissions during the period.



233  
234 **Figure 5. Extinction coefficient at 532 nm (a) and depolarization ratio (b) from 2154 LT on September 2nd,**  
235 **2020, to 0609 LT on September 3rd, 2020.**

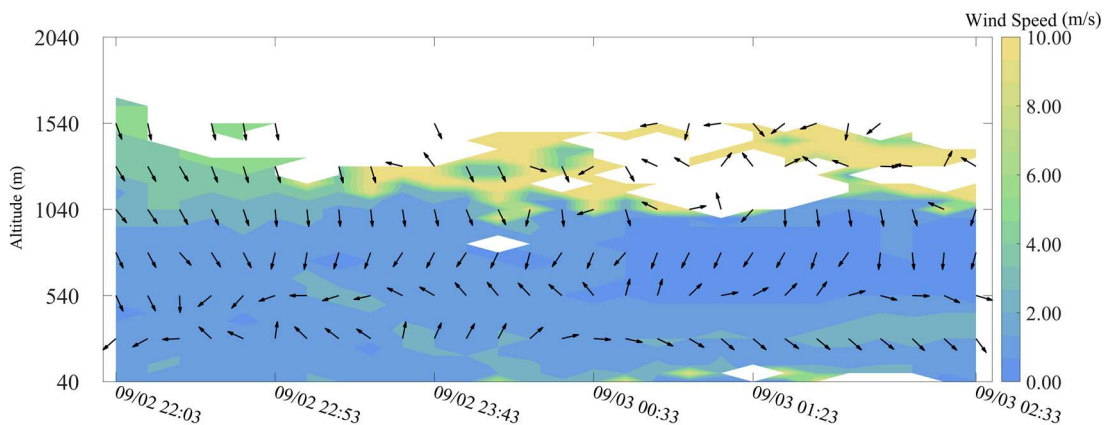
236

237 Figure 6 shows the horizontal wind speed and wind direction in this period. Noticeably, a light wind  
238 layer appeared below 1000 m, with horizontal wind speeds of each height maintained below 2 m/s.  
239 Such a static and stable condition was advantageous to the accumulation of locally generated  
240 particulate matter near the ground. However, light wind at higher altitude (500–1000 m) prevented the  
241 regional transport of particulate matter at a higher altitude, because it is difficult for such a low wind  
242 speed to blow the particulate matter at the corresponding height to the downstream area. Therefore,  
243 when light wind dominated near the ground, the particulate matter was likely to form a single layer on  
244 the surface.

245

246 It is worth noting that the wind at an altitude of 540 m at night gradually shifted to southerly wind,  
247 whereas the northerly weight of the 290 m altitude wind gradually increased. This shift in the wind was  
248 typical of a sea-land breeze in nocturnal coastal areas, which can only be observed when the  
249 background wind speed was relatively low.

250



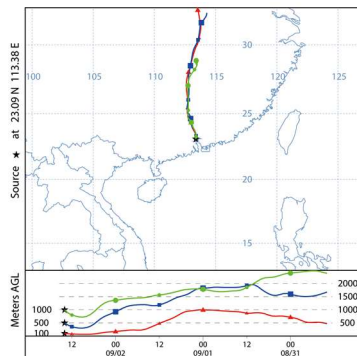
251

252 **Figure 6. Wind speed and wind direction of Type I. Colour map represents horizontal wind speed (m/s).**  
253 **Arrows represents the wind direction.**

254

255 The backward trajectories analysis of the same period (Figure 7) shows that on a large scale, the  
256 airflow in the boundary layer came from the north. The vertical trajectories of each layer were roughly  
257 parallel within 24 h, and all moved from high altitude to low, suggesting that particulate matter emitted  
258 near the ground in neighbouring cities was not easily transported by wind to Guangzhou.

259



260

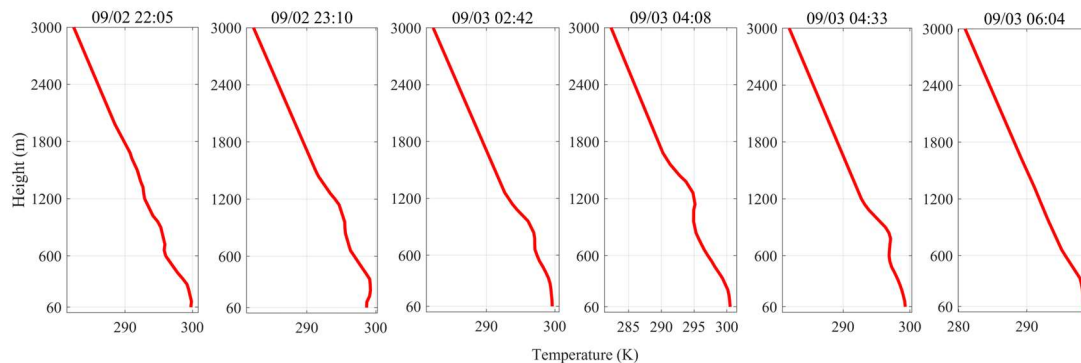
261 **Figure 7. Backward trajectories at 100 m, 500 m, and 1000 m, ending at 2200 LT September 2nd, 2020,**

262 determined by the HYSPLIT model.

263

264 Observations from the Raman temperature profile lidar (Figure 8) show an inversion between 600–  
265 1200 m before 0300 LT, which then rose to 1200 m and shrank to near the ground. Temperature  
266 inversion often exists at the top of the planetary boundary layer, trapping moisture and aerosols (Seibert  
267 et al., 2000). Hence, changes in the height of the inversion coincided with the trend of the top of the  
268 particulate matter layer on the vertical dimension revealed by MPL.

269

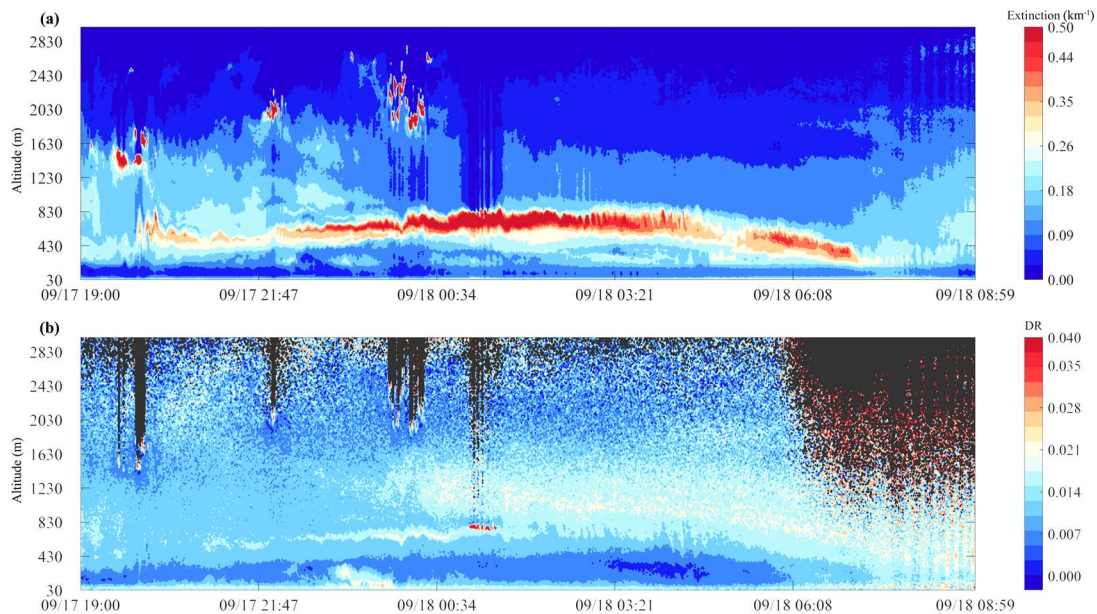


270

271 **Figure 8. Temperature profiles from the evening of September 2nd, 2020 to the early hours of September 3rd,**  
272 **2020.**

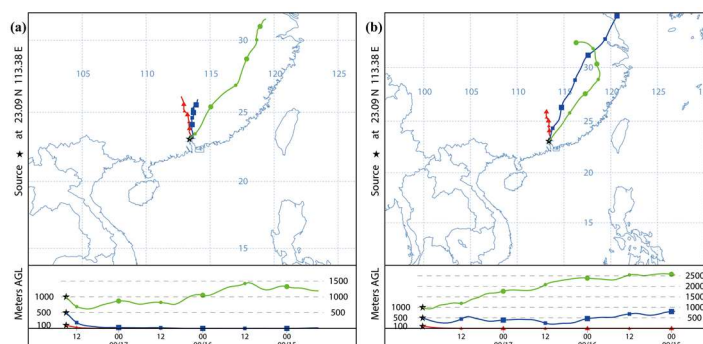
### 273 3.2.2 Type II: Elevated Single Layer

274 The particle layer was not only distributed near the ground but sometimes suspended at a higher  
275 altitude. Figure 9(a) shows the extinction coefficient time series of an elevated single layer of  
276 particulate matter. The low extinction coefficient near the ground suggests that it was clean below 400  
277 m during the night. The height of the high extinction coefficient layer gradually rose from 500–800 m  
278 at night, which then dropped below 400 m after dawn. The high value of the extinction coefficient  
279 corresponded to a higher depolarization ratio than the lower layer, which was approximately 0.02.  
280 However, the depolarization ratio of *Type II* was significantly lower than the depolarization ratio of the  
281 particle layer near the surface of *Type I*. This differing depolarization ratio was because local emissions  
282 dominated in *Type I*, and the primary pollutant emissions from anthropogenic sources near the surface  
283 with a non-spherical character and larger particle size accounted for a larger amount than that of *Type*  
284 *II*.  
285



286 **Figure 9. Extinction coefficient at 532 nm (a) and depolarization ratio (b) from 1900 LT on September 17th,**  
 287 **2019 to 0859 LT on September 18th, 2019.**  
 288

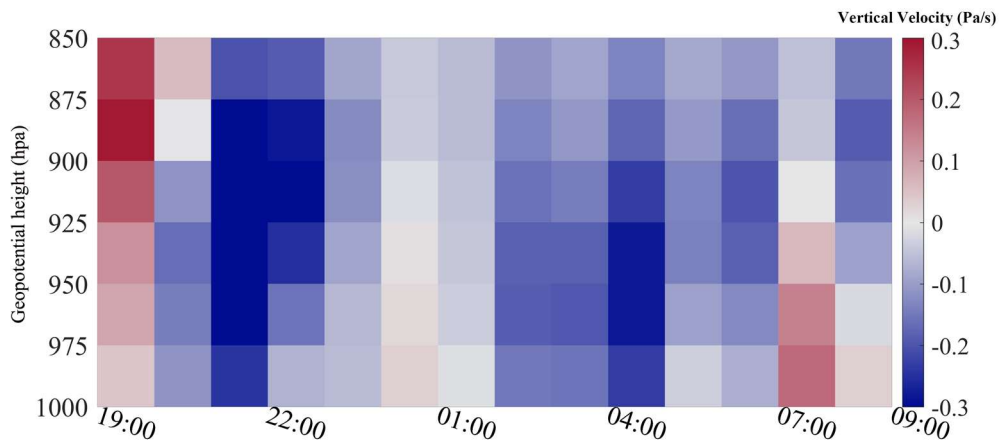
289  
 290 Figure 10(a) indicated that backward trajectories at 500 m and 100 m were both from near the ground,  
 291 elevating particles from lower levels vertically. Meanwhile, lower trajectories also carried particles  
 292 from the upper reaches of the region over Guangzhou horizontally. The domination of weak wind in the  
 293 boundary layer was beneficial to inter-city transport of particles. It brought particles from cities located  
 294 upstream to the location of our observation and allowed particles to stay longer without being blown  
 295 quickly downstream. In contrast, the trajectory at 1000 m came from a distance in the Y R D with a  
 296 larger wind speed, and the trajectory remained at a high altitude. Particles at 1000 m cannot stay for a  
 297 long time and were quickly transported downstream by strong winds. Hence, upward airflow near the  
 298 ground and vertical wind shear at a higher altitude were the causes of particulate matter forming an  
 299 elevated single layer. Unfortunately, the temperature profile and wind profile data were missing owing  
 300 to sampling failures. This upward convection of particles was confirmed by the ERA5 vertical velocity  
 301 reanalysis data of the corresponding time, shown in Figure 11.



303 **Figure 10. Backward trajectories at 100 m, 500 m, and 1000 m, ending at 2300 LT September 17th, 2019 (a)**  
 304 **and 0700 LT September 18th, 2019 (b), determined by the HYSPLIT model.**  
 305



308



309

310

Figure 11. ERA5 hourly vertical velocity from 1900 LT on September 17th, 2019, to 0900 LT on September 18th, 2019, at 23.25°N, 113.25°E. Negative values indicate upward motion.

312

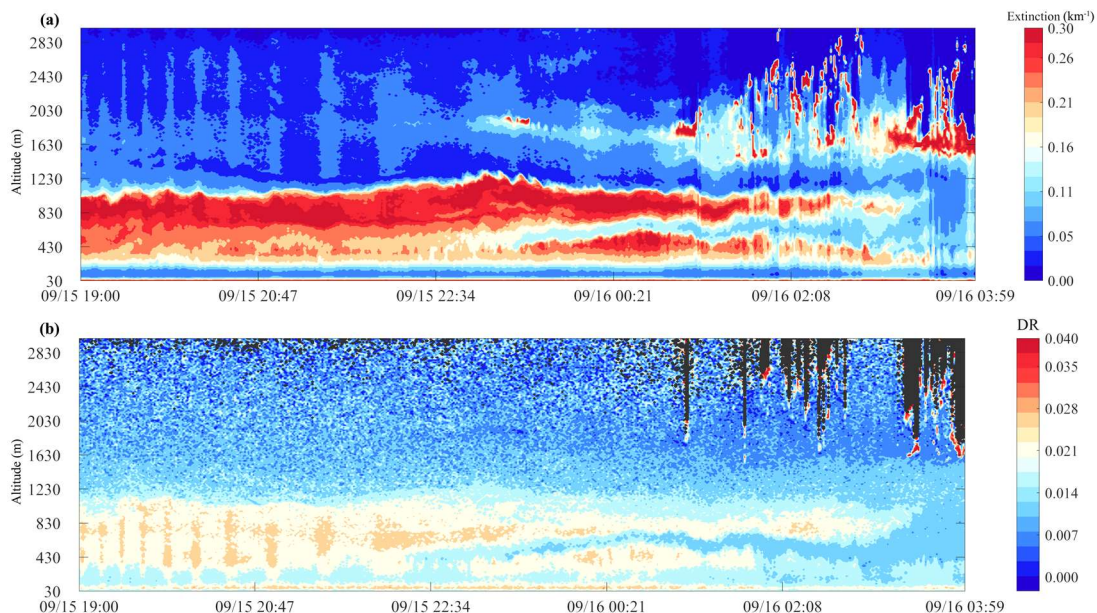
313

### 314 3.2.3 Type III: Double Layer

315

Figure 12 presents a thick single layer of particles transforming into a double layer structure. There was a layer concentrated near the ground after 2300 LT, along with another layer suspended at the height of 600–1000 m. A cleaner layer with a lower extinction coefficient existed between the two particle layers. The depolarization ratio of the suspending layer was higher than the layer near the surface, especially after 0100 LT, which indicated that sources of the two layers might be different.

320



321

322

Figure 12. Extinction coefficient at 532 nm (a) and depolarization ratio (b) from 1900 LT on September 15th, 2019 to 0359 LT on September 16th, 2019.

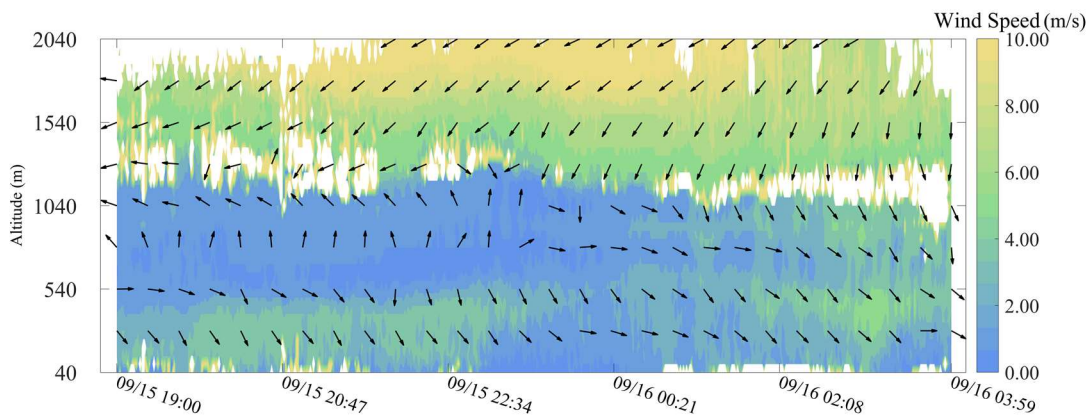
324

325

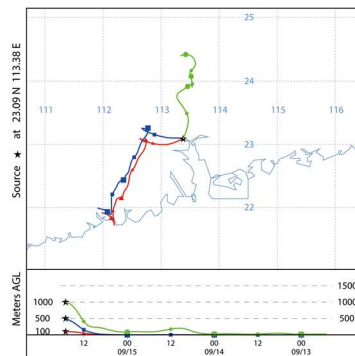
The vertical distribution of particulate matter was closely related to the horizontal wind speed at various heights (Figure 13). It can be seen that the wind speed of more than 1000 m increased

326

327 significantly with the altitude, reaching more than 6 m/s. By 2300 LT, the wind speed below 500 m was  
 328 approximately 4 m/s, obviously higher than the wind speed between 500–1000 m, and there were  
 329 significant differences in the wind direction. After 2300 LT, the wind speed near the ground decreased,  
 330 and wind direction gradually turned consistent with the upper level. The wind speed at 500 m  
 331 continued to be high, reaching 6 m/s maximumly. The layer with higher wind speed corresponded to  
 332 the height of the cleaner layer, which facilitated the transport of particulate matter downstream in a  
 333 horizontal direction. Figure 14 illustrates the backward trajectories when the double layer appeared. As  
 334 shown in Figure 14, the layer of particulate matter below 500 m may have originated in the southwest  
 335 of the GBA, whereas the layer of particulate matter at 1000 m may have originated from cities north of  
 336 the GBA area.



337  
 338 **Figure 13. Wind speed and wind direction of Type III.**  
 339

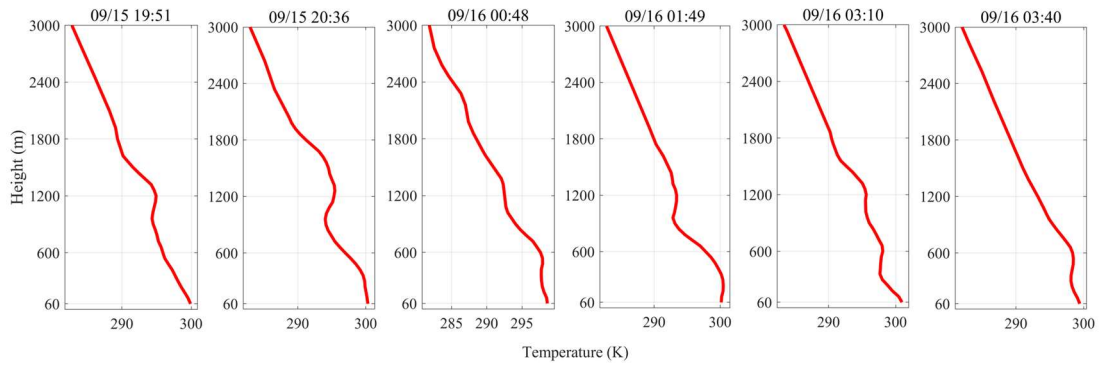


340  
 341 **Figure 14. Backward trajectories at 100 m, 500 m, and 1000 m, ending at 0100 LT September 16th, 2019,**  
 342 **determined by the HYSPLIT model.**  
 343

344 The vertical observations of the temperature (Fig. 15.) showed that on the night of September 15th,  
 345 2019, there was an inversion at 1200 m, which grew thicker. At 0048 LT, like the distribution of the  
 346 extinction coefficient, the inversion transformed into a double layer structure, with one remaining at  
 347 1200 m and another existing under 600 m. The vertical distributed double inversion, which allowed  
 348 particulate matter to concentrate at the corresponding height, resulted in a double layer distribution of  
 349 particulate matter.

350





351

352

**Figure 15. Temperature profiles from the evening of September 15th, 2019 to the early hours of September 16th, 2019.**

353

354

355

### **3.3 Effect of Meteorological Elements on the Distribution of Particles**

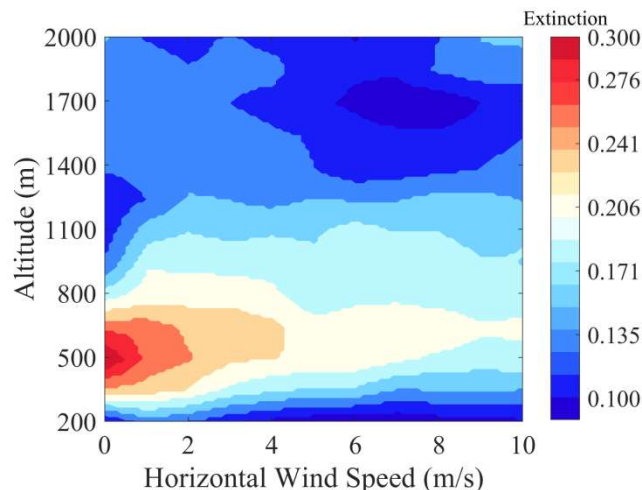
356

#### **3.3.1 Extinction Coefficient at Different Wind Speeds**

357

Using data of in situ observations during September and October of 2019 and 2020, statistics of average extinction coefficients at different altitudes and horizontal wind speeds were gathered, as shown in Figure 16. To eliminate the influence of clouds on the extinction coefficient, observations during cloudy weather were manually screened out based on the original signal of the MPL output and images of the sky above the field taken automatically by a camera. Because the spatial resolutions of the data from the two lidar are different, we interpolated the data to make them match each other vertically. The result shows that 500 m was the height with the highest average extinction coefficient, which indicated that the particle layer was most likely to appear at this height. The horizontal wind speed had different effects on the lower and upper parts of the boundary layer. Below 800 m, the extinction coefficient decreased as the wind speed increased, but it was the opposite above 800 m; i.e., the extinction coefficient increased with the wind speed. This altering of the extinction coefficient was because most of the particulate matter in the lower layer came from local emissions and easily accumulated in the presence of a layer with calm wind near the ground. However, in the upper layer, particulate matter was derived more from the surrounding areas, necessitating a certain minimum horizontal wind speed before it could be transported by the wind.

372



373

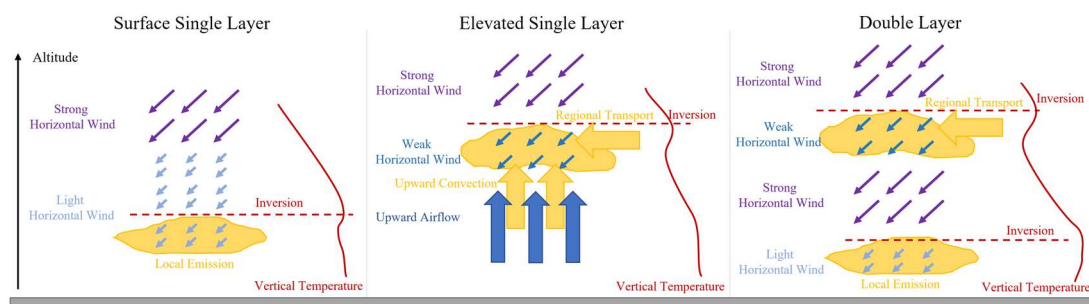
374 **Figure 16. Average extinction coefficient at different wind speeds and altitude from fixed-location**  
375 **observations of a total of 89 days at Haizhu Lake Research Base.**  
376

### 377 **3.3.2 Conceptual Model of Meteorological Elements and Vertical Distribution of Particles**

378 Based on the observational research above, a conceptual model was developed to summarise the effect  
379 of meteorological elements on the three typical vertical distributions of particles in the GBA.  
380

381 As shown in Figure 17, the surface single layer occurred when light horizontal wind dominated near  
382 the ground, which was not conducive to removing particles from local emissions. An elevated single  
383 layer was caused by upward airflow near the ground and vertical wind shear at a higher altitude. In this  
384 kind of wind structure, particle layer formation was dominated by upward convection and regional  
385 transport. A double layer existed because a layer with stronger horizontal wind existed between two  
386 layers with weaker wind, which facilitated the transport of particles from local emission and horizontal  
387 transport to downstream areas and resulted in a cleaner layer inside the polluted air mass.  
388

389 Another key factor that influenced the vertical distribution of particles was temperature inversion,  
390 which trapped most anthropogenic emissions from the surface, preventing them from penetrating out of  
391 the boundary layer. Furthermore, multiple inversions can cause more than one peak in the  
392 concentration of particles vertically.  
393



394

395 **Figure 17. Conceptual model of meteorological elements and vertical distribution of particles.**

396

## 397 **4. Conclusion**

398 The results of our study show how meteorological elements affected the three-dimensional distribution  
399 of particles in the western Guangdong–Hong Kong–Macao Greater Bay area. We focused mainly on  
400 the periods when the wet season changes to the dry season, as the frequently changing temperature and  
401 wind under such conditions have a more significant impact on the distribution of particles. The  
402 horizontal distribution of particles in the GBA was closely related to wind speed and wind direction.  
403 On days with stronger winds in the boundary layer, high values of AOD were mostly distributed in the  
404 downstream areas. On days with weaker winds, the horizontal distribution of particles in the GBA was  
405 homogeneous. The vertical distribution of particles in the GBA was classified into three typical types:  
406 surface single layer, elevated single layer, and double layer. The surface single layer occurred when

407 wind with very low speed dominated the boundary layer. The elevated single layer was caused by  
408 upward airflow near the ground and vertical wind shear at a higher altitude. The double layer existed  
409 because a layer with higher horizontal wind speed existed between two layers with weaker wind.  
410 Particles were concentrated near the temperature inversion. Multiple inversions can cause more than  
411 one peak in the vertical distribution of particulate matter. The mechanisms that affected the distribution  
412 of particulate matter in the upper and lower boundary layers are different. Lower horizontal wind speed  
413 was conducive to accumulating particulate matter near the ground, whereas higher horizontal wind  
414 speed promoted the transport of particles between surrounding areas in the upper boundary layer.

415

416 Further studies should be conducted during other seasons in the western Guangdong–Hong Kong–  
417 Macao Greater Bay Area to further verify the conceptual model of meteorological elements and vertical  
418 distribution of particles proposed in this article. In addition, more vertical observation instruments for  
419 meteorological elements, such as a radiometer, could be added to the multi-lidar system to further study  
420 the influence of the three-dimensional distribution of humidity, air pressure, and other meteorological  
421 elements on the distribution of particles.

422

#### 423 **Acknowledgments**

424 This work was supported by the National Natural Science Foundation of China (Grant No. 41630422)  
425 and the Guangdong Major Project of Basic and Applied Basic Research (Grant No.  
426 2020B0301030004).

427

#### 428 **References**

429

430 Dai, G., Wu, S., and Song, X.: Depolarization ratio profiles calibration and observations of aerosol  
431 and cloud in the Tibetan Plateau based on polarization Raman lidar, *Remote Sensing*, 10(3), 378,  
432 <https://doi.org/10.3390/rs10030378>, 2018.

433

434 Deng, T., Deng, X., Li, F., Wang, S., and Wang, G.: Study on aerosol optical properties and  
435 radiative effect in cloudy weather in the Guangzhou region, *Science of the Total Environment*,  
436 568, 147–154, <https://doi.org/10.1016/j.scitotenv.2016.05.156>, 2016.

437

438 Du, W., Zhang, Y., Chen, Y., Xu, L., Chen, J., Deng, J., Hong, Y., and Xiao, H.: Chemical  
439 characterization and source apportionment of PM<sub>2.5</sub> during spring and winter in the Yangtze  
440 River Delta, China, *Aerosol and Air Quality Research*, 17, 2165–2180,  
441 <https://doi.org/10.4209/aaqr.2017.03.0108>, 2017.

442

443 Fan, S., Liu, C., Xie, Z., Dong, Y., Hu, Q., Fan, G., Chen, Z., Zhang, T., Duan, J., Zhang, P., and  
444 Liu, J.: Scanning vertical distributions of typical aerosols along the Yangtze River using elastic  
445 lidar, *Science of The Total Environment*, 628, 631–641,  
446 <https://doi.org/10.1016/j.scitotenv.2018.02.099>, 2018.

447

448 Fang, X., Fan, Q., Li, H., Liao, Z., Xie, J., and Fan, S.: Multi-scale correlations between air quality  
449 and meteorology in the Guangdong–Hong Kong–Macao Greater Bay Area of China during 2015–  
450 2017, *Atmospheric Environment*, 191, 463–477, <https://doi.org/10.1016/j.atmosenv.2018.08.018>,

451 2018.  
452  
453 Fang, X., Fan, Q., Liao, Z., Xie, J., Xu, X., & Fan, S.: Spatial-temporal characteristics of the air  
454 quality in the Guangdong–Hong Kong–Macau Greater Bay Area of China during 2015–2017,  
455 *Atmospheric Environment*, 210, 14–34, <https://doi.org/10.1016/j.atmosenv.2019.04.037>, 2019.  
456  
457 Fernald, F. G.: Analysis of atmospheric lidar observations: some comments, *Applied optics*, 23,  
458 652–653, 1984.  
459  
460 He, Y., Wang, H., Wang, H., Xu, X., Li, Y., & Fan, S.: Meteorology and topographic influences on  
461 nocturnal ozone increase during the summertime over Shaoguan, China, *Atmospheric*  
462 *Environment*, 256, 118459, <https://doi.org/10.1016/j.atmosenv.2021.118459>, 2021b.  
463  
464 He, Y., Xu, X., Gu, Z., Chen, X., Li, Y., and Fan, S.: Vertical distribution characteristics of aerosol  
465 particles over the Guanzhong Plain, *Atmospheric Environment*, 255, 118444,  
466 <https://doi.org/10.1016/j.atmosenv.2021.118444>, 2021a.  
467  
468 Heese, B., Baars, H., Bohlmann, S., Althausen, D., and Deng, R.: Continuous vertical aerosol  
469 profiling with a multi-wavelength Raman polarization lidar over the Pearl River Delta, China,  
470 *Atmos. Chem. Phys.*, 17, 6679–6691, <https://doi.org/10.5194/acp-17-6679-2017>, 2017.  
471  
472 Huang T., Li Y., Cheng J.C.H., Haywood J., Hon K.K., Lam D.H.Y., Lee O.S.M., Lolli S.,  
473 O’Connor E.J., Lee H.F., Wang M., and Yim S.H.L.: Assessing Transboundary-local Aerosols  
474 Interaction over Complex Terrain Using a Doppler LiDAR Network, *Geophysical Research*  
475 *Letters*, 48,12, <https://doi.org/10.1029/2021GL093238>, 2021a.  
476  
477 Huang, T., Yang, Y., O’Connor, E. J., Lolli, S., Haywood, J., Osborne, M., Cheng. J. C. H. C.,  
478 Guo, J., and Yim, S. H. L.: Influence of a weak typhoon on the vertical distribution of air pollution  
479 in Hong Kong: A perspective from a Doppler LiDAR network, *Environmental Pollution*, 276,  
480 116534, <https://doi.org/10.1016/j.envpol.2021.116534>, 2021b.  
481  
482 Huige, D., Siwen, L., Yun, Y., and Dengxin, H.: Observational study of the vertical aerosol and  
483 meteorological factor distributions with respect to particulate pollution in Xi’an, *Atmospheric*  
484 *Environment*, 247, 118215, <https://doi.org/10.1016/j.atmosenv.2021.118215>, 2021.  
485  
486 Leikauf, G. D., Kim, S. H., and Jang, A. S.: Mechanisms of ultrafine particle-induced respiratory  
487 health effects, *Experimental & Molecular Medicine*, 52, 329–337, [https://doi.org/10.1038/s12276-](https://doi.org/10.1038/s12276-020-0394-0)  
488 [020-0394-0](https://doi.org/10.1038/s12276-020-0394-0), 2020.  
489  
490 Li, Y., Wang, B., Lee, S. Y., Zhang, Z., Wang, Y., and Dong, W.: Micro-Pulse Lidar Cruising  
491 Measurements in Northern South China Sea, *Remote Sensing*, 12, 1695,  
492 <https://doi.org/10.3390/rs12101695>, 2020.  
493  
494 Liao, Z., Gao, M., Sun, J., and Fan, S.: The impact of synoptic circulation on air quality and

495 pollution-related human health in the Yangtze River Delta region, *Science of the Total*  
496 *Environment*, 607, 838–846, <https://doi.org/10.1016/j.scitotenv.2017.07.031>, 2017.  
497

498 Liu, J., Wu, D., Fan, S., Mao, X., and Chen, H.: A one-year, on-line, multi-site observational study  
499 on water-soluble inorganic ions in PM<sub>2.5</sub> over the Pearl River Delta region, China, *Science of the*  
500 *Total Environment*, 601, 1720–1732, <https://doi.org/10.1016/j.scitotenv.2017.06.039>, 2017.  
501

502 Liu, Q., He, Q., Fang, S., Guang, Y., Ma, C., Chen, Y., Kang, Y., Pan, H., Zhang, H., and Yao, Y.:  
503 Vertical distribution of ambient aerosol extinctive properties during haze and haze-free periods  
504 based on the Micro-Pulse Lidar observation in Shanghai, *Science of the Total Environment*, 574,  
505 1502–1511, <https://doi.org/10.1016/j.scitotenv.2016.08.152>, 2017.  
506

507 Lu, X., Mao, F., Pan, Z., Gong, W., Wang, W., Tian, L., and Fang, S.: Three-dimensional physical  
508 and optical characteristics of aerosols over central china from long-term CALIPSO and HYSPLIT  
509 data, *Remote Sensing*, 10, 314, <https://doi.org/10.3390/rs10020314>, 2018.  
510

511 Lv, L., Liu, W., Zhang, T., Chen, Z., Dong, Y., Fan, G., Xiang, Y., Yao, Y., Yang, N., Chu, B.,  
512 Teng, M., and Shu, X.: Observations of particle extinction, PM<sub>2.5</sub> mass concentration profile and  
513 flux in north China based on mobile lidar technique. *Atmospheric Environment*, 164, 360–369,  
514 <https://doi.org/10.1016/j.atmosenv.2017.06.022>, 2017.  
515

516 Lv, L., Xiang, Y., Zhang, T., Chai, W., and Liu, W.: Comprehensive study of regional haze in the  
517 North China Plain with synergistic measurement from multiple mobile vehicle-based lidars and a  
518 lidar network, *Science of the Total Environment*, 721, 137773,  
519 <https://doi.org/10.1016/j.scitotenv.2020.137773>, 2020.  
520

521 Lyu, L., Dong, Y., Zhang, T., Liu, C., Liu, W., Xie, Z., Xiang, Y., Zhang, Y., Chen, Z., Fan, G.,  
522 Zhang, L., Liu, Y., Shi, Y., and Shu, X.: Vertical Distribution Characteristics of PM<sub>2.5</sub> Observed by  
523 a Mobile Vehicle Lidar in Tianjin, China in 2016, *Journal of Meteorological Research*, 32, 60–68,  
524 <https://doi.org/10.1007/s13351-018-7068-z>, 2018.  
525

526 Kim, H. C., Chai, T., Stein, A., and Kondragunta, S.: Inverse modeling of fire emissions  
527 constrained by smoke plume transport using HYSPLIT dispersion model and geostationary  
528 satellite observations, *Atmos. Chem. Phys.*, 20, 10259–10277, [https://doi.org/10.5194/acp-20-](https://doi.org/10.5194/acp-20-10259-2020)  
529 10259-2020, 2020.  
530

531 Orru, H., Ebi, K. L., and Forsberg, B.: The interplay of climate change and air pollution on health,  
532 *Current environmental health reports*, 4, 504–513, <https://doi.org/10.1007/s40572-017-0168-6>,  
533 2017.  
534

535 Seibert, P., Beyrich, F., Gryning, S. E., Joffre, S., Rasmussen, A., and Tercier, P.: Review and  
536 intercomparison of operational methods for the determination of the mixing height, *Atmospheric*  
537 *Environment*, 34, 1001–1027, [https://doi.org/10.1016/S1352-2310\(99\)00349-0](https://doi.org/10.1016/S1352-2310(99)00349-0), 2000.  
538

539 Sekula, P., Bokwa, A., Bartyzel, J., Bochenek, B., Chmura, L., Galkowski, M., and Zimnoch, M.:  
540 Measurement report: Effect of wind shear on PM<sub>10</sub> concentration vertical structure in the urban  
541 boundary layer in a complex terrain, *Atmos. Chem. Phys.*, 21, 12113 – 12139,  
542 <https://doi.org/10.5194/acp-21-12113-2021>, 2021.

543

544 Shao, Q., Liu, X., and Zhao, W.: An alternative method for analyzing dimensional interactions of  
545 urban carrying capacity: case study of Guangdong–Hong Kong–Macao Greater Bay Area, *Journal*  
546 *of Environmental Management*, 273, 111064, <https://doi.org/10.1016/j.jenvman.2020.111064>,  
547 2020.

548

549 Stocker, T. (Ed.): *Climate change 2013: the physical science basis: Working Group I contribution*  
550 *to the Fifth assessment report of the Intergovernmental Panel on Climate Change*, Cambridge  
551 university press, 2014.

552

553 Strawa, A. W., Kirchstetter, T. W., Hallar, A. G., Ban-Weiss, G. A., McLaughlin, J. P., Harley, R.  
554 A., and Lunden, M. M.: Optical and physical properties of primary on-road vehicle particle  
555 emissions and their implications for climate change, *Journal of Aerosol Science*, 41, 36–50,  
556 <https://doi.org/10.1016/j.jaerosci.2009.08.010>, 2010.

557

558 Tian, P., Cao, X., Zhang, L., Sun, N., Sun, L., Logan, T., Shi, J., Wang, Y., Ji, Y., Lin, Y., Huang,  
559 Z., Zhou, T., Shi, Y., and Zhang, R.: Aerosol vertical distribution and optical properties over China  
560 from long-term satellite and ground-based remote sensing, *Atmos. Chem. Phys.*, 17, 2509–2523,  
561 <https://doi.org/10.5194/acp-17-2509-2017>, 2017.

562

563 Wallace, J., and Kanaroglou, P.: The effect of temperature inversions on ground-level nitrogen  
564 dioxide (NO<sub>2</sub>) and fine particulate matter (PM<sub>2.5</sub>) using temperature profiles from the Atmospheric  
565 Infrared Sounder (AIRS), *Science of the Total Environment*, 407, 5085–5095,  
566 <https://doi.org/10.1016/j.scitotenv.2009.05.050>, 2009.

567

568 Wang, H., Sun, Z., Li, H., Gao, Y., Wu, J., and Cheng, T: Vertical-distribution characteristics of  
569 atmospheric aerosols under different thermodynamic conditions in Beijing, *Aerosol and Air*  
570 *Quality Research*, 18(11), 2775–2787, <https://doi.org/10.4209/aaqr.2018.03.0078>, 2018.

571

572 Xie, J., Liao, Z., Fang, X., Xu, X., Wang, Y., Zhang, Y., Liu, J., Fan, S., and Wang, B.: The  
573 characteristics of hourly wind field and its impacts on air quality in the Pearl River Delta region  
574 during 2013–2017, *Atmospheric Research*, 227, 112–124,  
575 <https://doi.org/10.1016/j.atmosres.2019.04.023>, 2019.

576

577 Xu, Y., Xue, W., Lei, Y., Zhao, Y., Cheng, S., Ren, Z., and Huang, Q.: Impact of meteorological  
578 conditions on PM<sub>2.5</sub> Pollution in China during winter, *Atmosphere*, 9, 429,  
579 <https://doi.org/10.3390/atmos9110429>, 2018.

580

581 Yao, L., Zhan, B., Xian, A., Sun, W., Li, Q., and Chen, J.: Contribution of transregional transport  
582 to particle pollution and health effects in Shanghai during 2013–2017, *Science of the Total*



583 Environment, 677, 564-570, <https://doi.org/10.1016/j.scitotenv.2019.03.488>, 2019.s  
584  
585 Zang, Z., Wang, W., You, W., Li, Y., Ye, F., and Wang, C.: Estimating ground-level PM<sub>2.5</sub>  
586 concentrations in Beijing, China using aerosol optical depth and parameters of the temperature  
587 inversion layer, *Science of the Total Environment*, 575, 1219–1227,  
588 <https://doi.org/10.1016/j.scitotenv.2016.09.186>, 2017.  
589  
590 Zhao, Y. F., Gao, J., Cai, Y. J., Wang, J. J., and Pan, J.: Real-time tracing VOCs, O<sub>3</sub> and PM<sub>2.5</sub>  
591 emission sources with vehicle-mounted proton transfer reaction mass spectrometry combined  
592 differential absorption lidar, *Atmospheric Pollution Research*, 12(3), 146-153,  
593 <https://doi.org/10.1016/j.apr.2021.01.008>, 2021.  
594  
595 Zhou, Y., Shan, Y., Liu, G., and Guan, D.: Emissions and low-carbon development in Guangdong-  
596 Hong Kong-Macao Greater Bay Area cities and their surroundings, *Applied energy*, 228,  
597 1683–1692, <https://doi.org/10.1016/j.apenergy.2018.07.038>, 2018.  
598